引用格式：WANG Luqiang, PU Tao, LI Jin, et al. Advanced Over-the-horizon Communications with Microwave Photonic Technologies (Invited)[J]. Acta Photonica Sinica, 2026, 55(3):0355110
王路强,蒲涛,李晋,等. 基于微波光子学的先进超视距通信技术研究(特邀)[J].光子学报,2026,55(3):0355110

基于微波光子学的先进超视距通信技术研究（特邀）

王路强[1,2],蒲涛[1],李晋[1],郑吉林[1],周华[1],赵小龙[1],刘淑雅[1],于净曦[2]
(1 中国人民解放军陆军工程大学,南京 210001)
(2 中国电子科技集团公司第五十四研究所,石家庄 050002)

摘　要:设计并构建了基于微波光子技术的超视距通信系统架构,解析了系统工作机制,通过链路仿真验证了技术可行性,实现了超视距通信系统在4～16 GHz带宽范围内的信号传输,通信速率达200 Mbps,并具备13个波道的可重构微波光子信道化变频能力,为微波光子技术在超视距通信系统中的工程化应用奠定了重要基础。

关键词:微波光子;超视距通信;相控阵;光频梳;变频
中图分类号:TN914　　**文献标识码**:A　　**doi**:10.3788/gzxb20265503.0355110

0 引 言

传统超视距通信系统主要基于微波技术实现,其工作原理是在发射端将电能转换为特定频率的高频微波振荡信号并辐射至自由空间,接收端则通过定向天线捕获微弱微波信号,经放大与解调后还原出原始信息[1]。由于微波信号在空间传播过程中受路径损耗与大气衰减影响显著,接收信号的信噪比较低,而且此类系统通常只能采用窄带宽、大功率、点对点的传输机制[2],其在通信容量、传输速率、抗干扰与抗截获能力等方面存在电子瓶颈,难以满足未来信息化对超视距通信系统的高要求[3]。

微波光子学是一门研究微波与光子相互作用及应用的交叉学科[4-7],它结合了微波技术和光子技术的优势,实现了微波信号在光域中的传输和处理。微波光子技术,作为一种在光域中实现对微波信号的生成、传输、控制以及处理的前沿技术,具有光子学高频段、大带宽、低损耗、体积小、重量轻和抗电磁干扰等优势[8],能够克服传统微波系统在高频段、超宽带、多通道并行处理、智能抗干扰等方面的电子瓶颈。近年来,微波光子学在雷达[9-15]与卫星通信[16-20]领域取得了显著进展,相关技术研究涵盖了基于微波光子的多波段雷达[9-10,14]、光频率梳信道化[12,15]、超宽带卫星通信[16-17]以及星载光子下变频[18-20]等多个方向,这也为超视距通信系统的创新发展提供了重要的技术支撑和理论指导。

国内外已经发表了很多将微波光子网络应用于相控阵雷达的报道,其核心在于利用光子技术来实现相控阵天线所需的波束形成与扫描功能。文献[21]利用微波光子网络实现了2～4 GHz的相控阵雷达,文献[22]相控阵使用基于微波光子学的馈电网络实现了在12～17 GHz范围内频率扫描,但这两种方法实现的频率范围较窄;文献[23]介绍一种集成微波光子雷达相控阵系统,大大降低了雷达的体积,但是实现复杂度较高,难以工程化应用;文献[11]提出了一种混合数模微波光子学波束赋形架构,前端数字模块以不同的斜率生成相位编码微波波形,而后端模拟模块使用固定的光学真实时间延迟对准波束成形,以实现波束的多方向指向,虽然提高了扫描精度,但是光束切换控制比较困难。

基金项目:国家自然科学基金(62201615, 62371470)
第一作者:王路强,wlq_cetc@163.com
通讯作者:蒲涛,nj_putao@163.com
收稿日期:2025-11-30;**录用日期**:2026-01-15

光频梳(Optical Frequency Comb, OFC)凭借其高相干性和低相位噪声等优良特性,也受到了越来越多学者的广泛关注,由于其能够同时提供多个高精度的相干光载波,为微波频率变换提供了新的技术路径。文献[24]利用OFC成功将2~20 GHz的微波信号下变频至中频;文献[25]通过双光频梳仿真实现了15 GHz Ku波段信号向3~27 GHz多信道频率的转换;文献[26]则采用17根梳齿的OFC完成了25.5~40.0 GHz mm波信号的下变频。然而,受限于光频梳的梳齿质量、滤波带宽等因素,目前这些方法主要应用于下变频场景,在应用范围和灵活性方面仍存在一定局限。

因此,本文基于微波光子学提出了一种新型超视距通信系统架构,通过引入64阵元微波光子链路实现相控阵[27]天线信号相干功能,采用双光频梳技术[28]实现可重构信道化变频功能,赋予超视距通信系统高带宽、大容量、强抗干扰通信能力。并利用OptiSystem15.0软件对所提架构中的64阵元微波光子相控阵链路及光频梳上变频链路进行仿真验证。结果表明,该系统可实现4~16 GHz带宽范围内的信号传输,通信速率达200 Mbps,并具备13个波道的可重构微波光子信道化变频能力,为超视距通信系统的发展提供了有效技术路径。

1 基本原理

新型超视距通信系统主要由微波光子相控阵天线阵列、微波光子变频单元和综合通信终端组成,如图1所示。其中,微波光子相控阵天线阵列采用64阵元,同时接收来自自由空间的无线信号,之后将射频信号送至低噪声放大器(Low-Noise Amplifier, LNA)组件内进行放大,放大后的信号进入直调激光器(Directly Modulated Laser, DML)调制到光信号;光信号进入延迟衰减器,通过控制单元控制64阵元延迟衰减通道的衰减和延时,然后通过波分复用(Wavelength Division Multiplexing, WDM)进行波束合成,合成后的光信号经光电探测器(Photodetector, PD)转换为电信号送入变频单元,经过外调制(Electro-optic modulation, EOM),并结合OFC实现射频信号的下变频,最后将光信号转化为基带电信号,在综合处理终端(Integrated Communications Terminal, ICT)进行解调、译码、协议处理等,恢复出传输的业务信息。

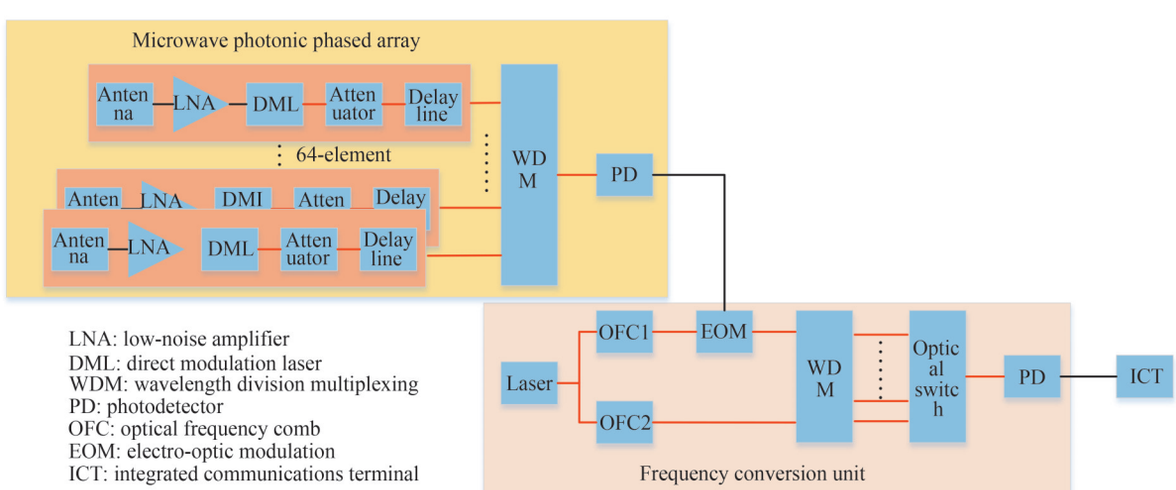

图1 超视距通信系统架构图

Fig.1 Architectural diagram of over-the-horizon communication system

1.1 微波光子相控阵天线链路信噪比分析

本文采用的微波光子相控阵天线基于微波光子真延时波束赋形技术,在光域对阵列天线接收信号因入射方向差异引入的时延进行补偿[29];所采用的真延时技术具有与微波频率无关的特性,特别适用于超宽带覆盖及超高速捷变射频信号的通信需求[30]。系统在光域利用可调光延迟线阵列对已调光信号进行延时控制,从而实现各天线接收信号的时延匹配与时域精确对齐,完成波束赋形[31],提升了链路的接收增益。

1)链路增益计算

按照图1微波光子相控阵部分所示的信号流程,64阵元天线接收到射频信号后先经两级LNA实现接收

信号的放大，然后直接调制加载在64路不同波长的光载波上，而后通过64路光域延时单元和64路光域衰减单元，随后通过WDM将64路光信号合束后经过PD输出。每路天线阵元输入信号为－95 dBm～－75 dBm，经过两级LNA放大60 dB后，输入DML信号功率为－35 dBm～－15 dBm，对应电流0.11 mA～1.12 mA。按照一般商用激光器的性能参数，取激光器阈值电流为10 mA，直流偏置为25 mA，调制斜率为0.25 W/A，输出的交流光功率为3.78 mW～4.03 mW（5.77 dBm～6.05 dBm）。经过延时衰减网络3 dB插损、波分复用器7 dB插损后，到达WDM的交流光功率为－4.23 dBm～－3.95 dBm。

8路不同波长的直调光在非相干耦合后有9 dB增益，经WDM合路后的光功率为4.77 dBm～5.05 dBm，PD响应度设置为1.0 A/W，射频信号功率为－6.47 dBm～－5.92 dBm，考虑PD输出为并联模型，最终链路输出的射频信号功率为－12.47 dBm～－11.92 dBm。

8组8路矩阵单元通过插损为2dB的耦合器实现合路，合成为64路后的光功率输出为11.77 dBm～12.05 dBm，PD响应度为1.0 A/W，射频信号功率为7.52 dBm～8.08 dBm，考虑PD输出为并联模型，最终链路输出的射频信号功率为1.52 dBm～2.08 dBm。

2）噪声功率分析

微波光链路中的噪声源主要包括热噪声、相对强度噪声和散粒噪声。热噪声主要来自链路中的各种电阻元件的热运动[32]；散粒噪声是主要来自光电二极管的噪声，是由光子转换成自由电子时的间断性造成的[33]；相对强度噪声主要说明了激光器的性能，表示激光器输出功能的波动值[34]。

为降低链路噪声系数，需提高激光器的转换效率并改善其相对强度噪声性能；同时，降低链路中的光电流（即直流偏置功率）也有助于减小系统噪声系数[35]。然而，直流偏置功率的降低会压缩系统动态范围，影响链路整体性能，因此需对其取值进行权衡分析[36]。链路中随着系统频率升高，链路固有增益会下降，噪声系数也相应增大[37]。基于上述分析，本文选取了经过优化的参数组合进行噪声功率计算。

系统的光链路噪声总共包含四个部分，包括热噪声、暗电流噪声、RIN噪声以及散粒噪声。其中接收机热噪声为－174 dBm/Hz。将暗电流约为4 nA带入式（1）。

$$P_{\mathrm{dark}}=\frac{1}{2}qI_{\mathrm{D}}BR \tag{1}$$

式中，P_{dark}为光电探测器的噪声功率，q为基本电荷常数，I_{D}为暗电流，B为带宽，R为阻抗，经过计算光电探测器的噪声功率为1.6×10^{-26} W，可见系统的热噪声和散粒噪声在最终总噪声功率输出中所占比重较小。考虑RIN噪声为－145 dBc/Hz，单路PD前光功率为－6 dBm，根据式（2）可计算出RIN噪声功率。

$$P_{\mathrm{RIN}}=<I_{\mathrm{RIN}}^{2}>R=\mathrm{RIN}(\eta P_{\mathrm{IN}})^{2}BR \tag{2}$$

式中，P_{RIN}为RIN噪声功率，$<I_{\mathrm{RIN}}{}^{2}>$为RIN噪声电流均方值，η为光电探测器的响应度，P_{IN}为入射到光电探测器的光功率，经计算RIN噪声功率为1.25×10^{-20} W，合路后噪声有18 dB增益。由于合路后PD前光功率约为12 dBm，带入式（3），计算得到散粒噪声功率为6.34×10^{-21} W。

$$P_{\mathrm{shot}}=\frac{1}{2}q(\eta P_{\mathrm{IN}})BR \tag{3}$$

式中，P_{shot}为散粒噪声功率。根据式（4），计算出总噪声功率为2.28×10^{-20} W。

$$P_{\mathrm{noise\_opt}}=P_{\mathrm{the}}+P_{\mathrm{RIN}}+P_{\mathrm{dark}}+P_{\mathrm{shot}} \tag{4}$$

式中，$P_{\mathrm{nosie_opt}}$为总噪声功率，P_{the}为热噪声功率。

天线接收信号的噪声为－174 dBm/Hz，经过级联噪声系数为2 dB、放大倍数分别为35 dB和25 dB的LNA。根据上文的功率预算，从天线输出到PD输出的链路增益为77.08 dB，单路链路增益为77.08－36＝41.08 dB。

所以，天线接收信号的噪声经光链路，再叠加光链路噪声功率后，得到系统总噪声功率为－71 dBm/Hz。考虑信号带宽为10 MHz，以噪声带宽20 MHz计算系统总噪声功率为7.94×10^{-11}W。

根据上文的功率预算，每路天线阵元输入信号为－95 dBm～－75 dBm，以输入信号为－75 dBm计算，输入信噪比为8.58 dB，经过光链路最终输出射频信号功率为2.08 dBm，链路增益约77 dB。考虑此时信号带宽为10 MHz，以噪声带宽为20 MHz，计算出总噪声功率为－78 dBm@20 MHz，整个输出链路的信噪比大于5 dB。

1.2 光频梳上下变频原理分析

本文利用相干双光频梳技术来精准实现中频信号(336 MHz)、射频信号(4~16 GHz)的上下变频。光频梳上变频原理如图2所示,上支路采用EOM结合直接数字合成器(Direct Digital Synthesizer, DDS)完成本振(Local Oscillator, LO)OFC在小范围内的频率移动,实现本振光频梳的精准频移;下支路则通EOM,在信号光频梳(OFC1)上实现中频(Intermediate Frequency, IF)信号的光域加载。射频与本振之间的连接通过光路隔开,并通过调节电光调制器的工作偏置点,确保电光调制器工作在载波抑制单边带状态,从而确保了无本振泄露,提供了极高的隔离度。然后链路经过光波分复用,实现多频段、多信道同时并行变频。光频梳下变频原理如图3所示,上支路选出的光信号被DDS产生的小偏移量电信号进行调制,偏移量大小由控制单元控制,作为通道内小跨度变频本振源;下支路通道选择的光信号作为光载波,通过电光调制加载4-16 GHz的射频(Radio Frequency, RF)信号;然后经过光耦合器,上支路的LO与下支路的信号光信号(OFC2)合路到一起并经过光电转换,可实现4~16 GHz带宽工作范围内的超宽RF信号到IF信号的精准下变频。

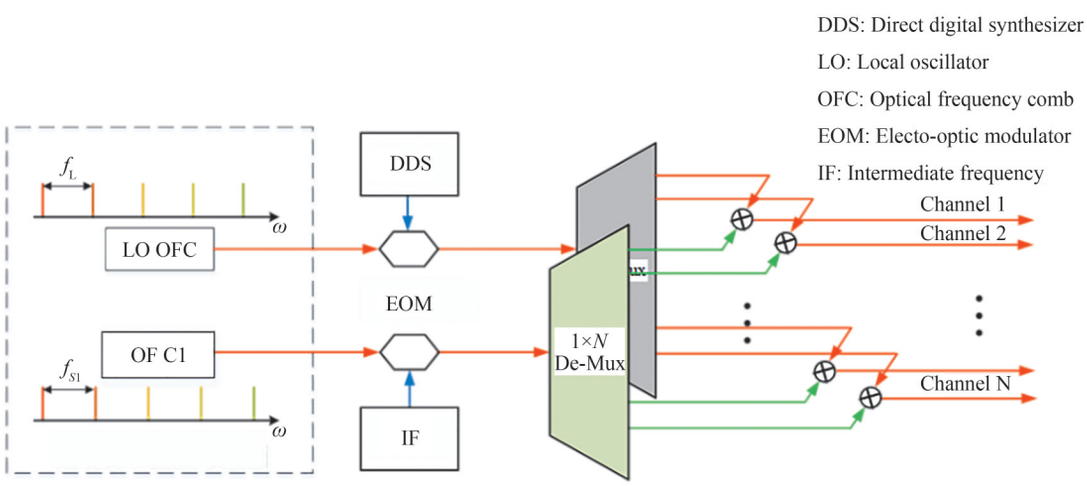

图2 光频梳上变频原理图

Fig.2 Schematic diagram of optical frequency comb up-conversion

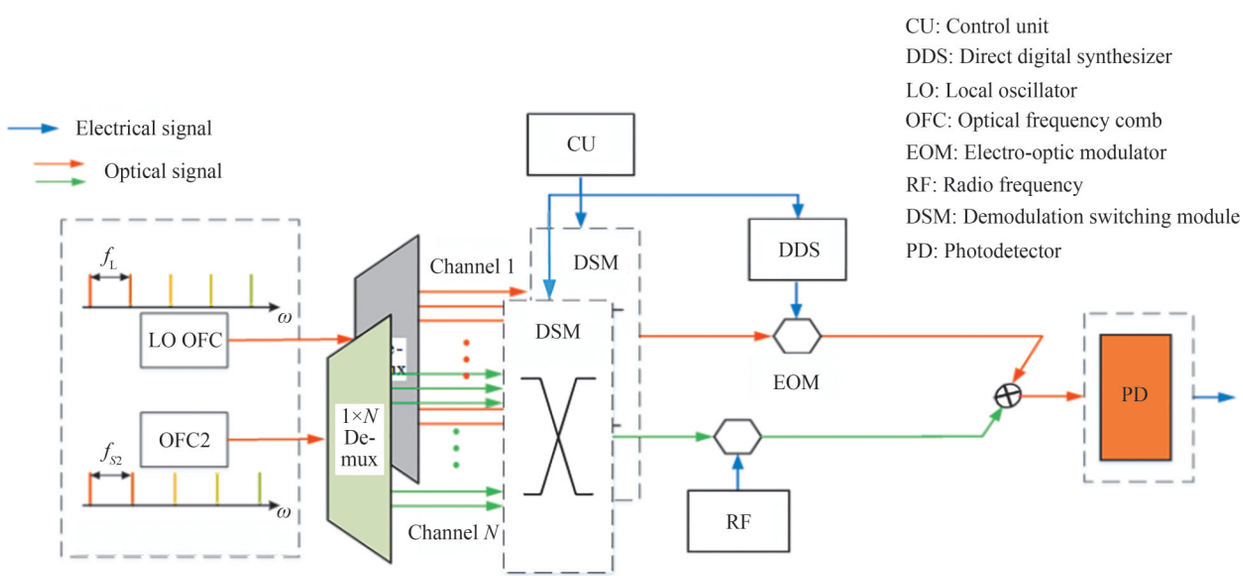

图3 光频梳下变频原理图

Fig.3 Schematic diagram of optical frequency comb down-conversion

2 仿真分析

2.1 微波光子相控阵天线链路

本文利用Optisystem15.0仿真软件搭建系统接收端的射频电路仿真模型，分别搭建了8阵元、64阵元的仿真链路。根据现有商用光学器件的指标能力，在仿真软件中对相关器件的参数进行设置。64阵元光信号中心波长为1 528.77 nm～1 579.52 nm，对应的频率为189.8 THz～196.1 THz，搭建的8阵元仿真模型选择193.1 THz～193.8 THz作为激光器的中心波长。对于其他器件，相对强度噪声设置为－144 dB/Hz、阈值电流10 mA、激光器的调制斜率0.25 W/A、偏置电流40 mA。探测器响应度1.06 A/W、暗电流4 nA、热噪声2×10^{-11} A/Hz$^{1/2}$。延迟衰减网络插损为3 dB，波分复用器插损为7 dB。

先搭建了8阵元链路，如图4所示。将接收到的带有200 MHz带宽信息的射频信号通过两级LNA放大，然后分为8路，每一路分别进DML，将射频信号直接调制到光信号，之后进入衰减延时网络，对信号进行时延处理后，进入波分复用进行合路，合路后通过光电探测器进行光电转换，输出射频信号。

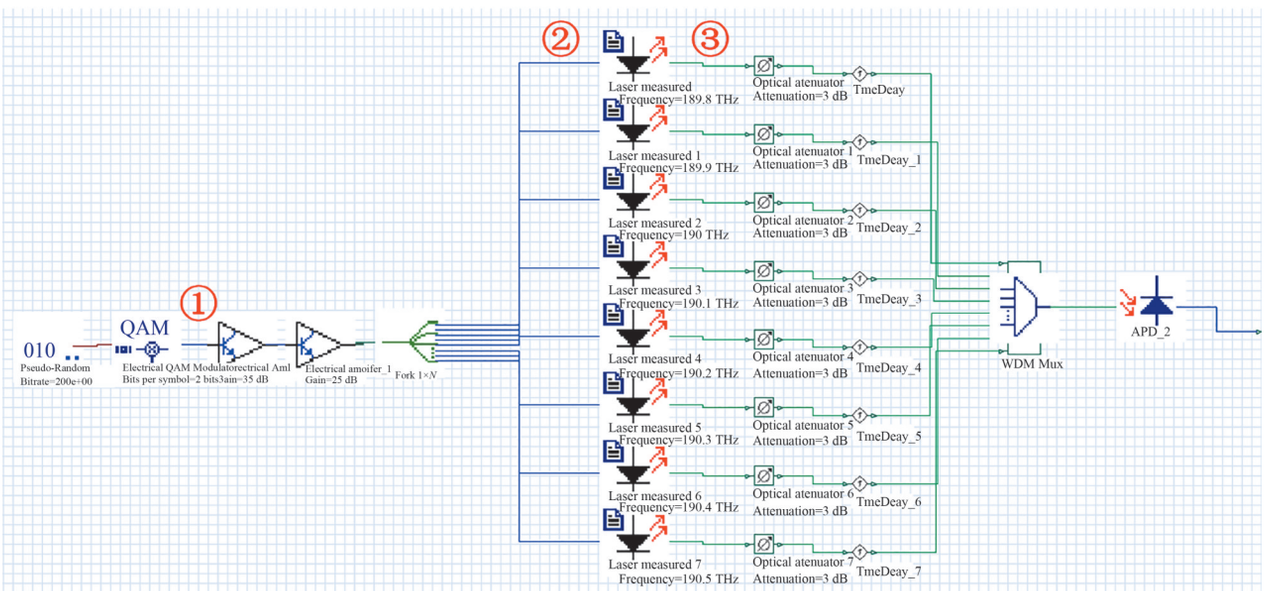

图4 8路仿真结构图

Fig.4 8-channel simulation schematic diagram

由仿真结果得到：输入DML的射频信号频率为4 GHz，天线接收到的信号功率为－75.51 dBm，如图5(a)所示，此射频信号带宽为100 MHz，其频谱图如图6(a)所示。经调制后，其输出光功率为5.62 dBm，如图5(b)所示，直调激光器的光谱图如图6(b)所示。经过光电探测器后输出的射频信号功率为－24.76 dBm，如图5(c)所示。通过LNA放大后，最终输出的射频信号功率为1.29 dBm，如图5(d)所示。8阵元相控阵链路增益为76.80 dBm。

图5 仿真测试功率输出。(a)天线接收信号功率；(b)激光器输出功率；(c)拍频后输出信号功率；(d)最终输出信号功率

Fig.5 Simulated power outputs. (a) Antenna received signal power; (b) Laser output power; (c) Output signal power after heterodyning; (d) Final output signal power

对8阵元链路的误差向量幅度(EVM)进行了仿真分析，得到输入射频信号和输出射频信号的EVM结果分别如图7(a)、(b)所示，根据信噪比与EVM之间的近似计算公式SNR≈－20 lg(EVM)，计算出链路前后的信噪比分别为：8.58 dB、8.22 dB，噪声系数为0.36 dB。

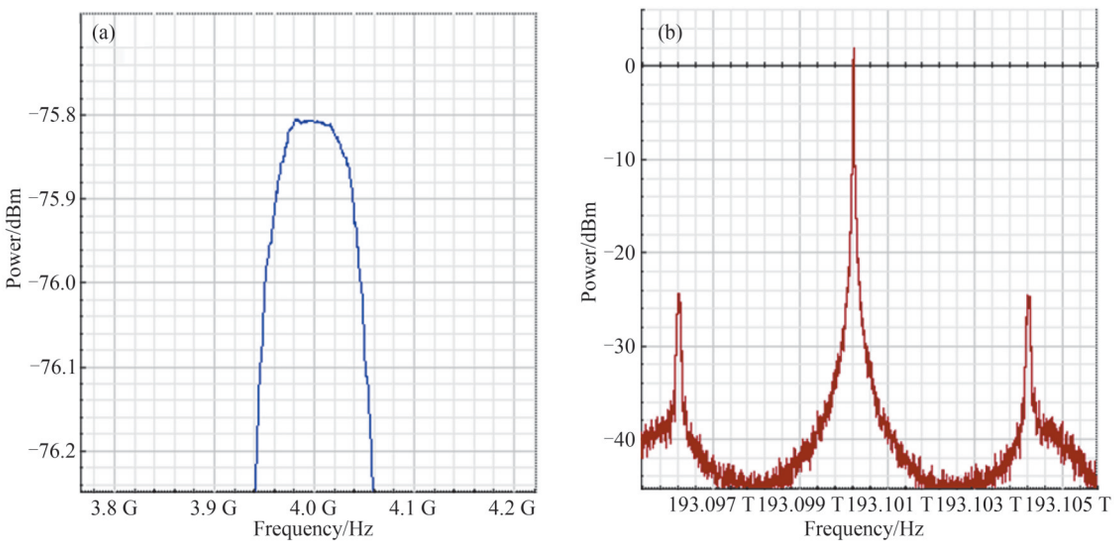

图 6 信号频谱图。(a)天线接收信号频谱图;(b)激光器输出信号频谱图

Fig.6 Signal spectrum diagrams. (a) Antenna received signal spectrum; (b) Laser output signal spectrum

Results (a)

Disp	Name	Value
☐	Log of estimated symbo	−2.06702555022883
☐	Estimated symbol error	0.008569874258263
☐	Q factor from estimate	2.624029070809454
☐	Error vector magnitude	0.372251783252773

Results (b)

Disp	Name	Value
☐	Log of estimated symb	−2.042912929586811
☐	Estimated symbol error	0.0090591420674646
☐	Q factor from estimate	2.606765721659392
☐	Error vector magnitude	0.3880510884365707

图 7 8阵元链路传输前后射频信号的EVM数值。(a)传输前;(b)传输后

Fig.7 EVM Values of RF signals before and after 8-element link transmission. (a) Before transmission; (b) After transmission

为了利于对单链路性能指标的仿真分析,将64阵元分为8个子模块,即1个子模块包含8阵元仿真链路,通过先对其中1个子模块中的8阵元进行仿真分析,然后将8个子模块通过耦合器结合到一起(加上耦合增益),便构成64阵元仿真链路,如图8所示。

链路合路后的光功率如图9(a)所示,光电探测器直接输出的射频信号功率如图9(b)所示,64阵元链路输出射频信号的EVM结果,如图10所示,通过分析计算可以得到链路传输后的信号信噪比为5.67 dB,链路的噪声系数为2.91 dB。

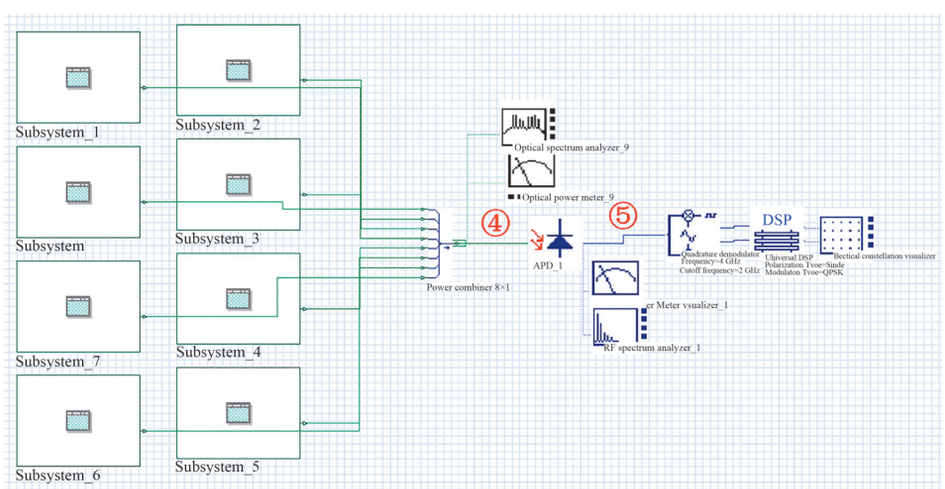

图 8 64阵元仿真结构图

Fig.8 64-Element simulation schematic diagram

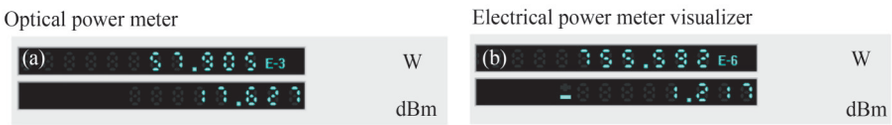

图 9　64 阵元合路后的结果。(a)光功率；(b)输出射频信号功率

Fig.9　Result of after 64-element combining (a) Optical power; (b) Output RF signal power

Results

Disp	Name	Value
☐	log of estimated symbo	-1000
☐	Estimated symbol error	0
☐	Q factor from estimate	10e+099
☐	Error vector magnitude	0.5208397745042342

图 10　64 阵元链路传输后射频信号的 EVM 数值

Fig.10　EVM values of RF signals after 64-element link transmission

下面以链路输入射频信号功率－75 dBm 为例，对 64 阵元链路中各节点的理论与仿真结果进行对比分析，结果如表 1 所示，其中位置①-⑤是在仿真链路中设置的仿真节点，位置①②③如图 4 所示，①表示输入 LNA 前的信号，②表示输入 DML 前的信号，③表示经过 DML 后的信号；位置④⑤如图 8 所示，④表示信号经过 64 路合路后的信号，⑤表示经过 PD 输出后的信号。从表中可以看出，仿真结果与理论计算结果基本相符合，但出现了一些偏差，可能是由于仿真中直调激光器的相对强度噪声以及光电探测器的散粒噪声、电容等因素的影响。下一步工作将对光学器件参数对链路增益、带宽、信噪比等指标的影响进行深入研究，通过分析影响链路的主要指标，对指标进行权衡和优化，使得链路达到相对最佳的性能。

表 1　64 阵元链路各节点理论计算与仿真结果对比

Table 1　Comparison of theoretical and simulation results for 64-element link nodes

Position	Theoretical power/dBm	Simulated power/dBm	Signal-to-noise ratio/dB
①	－75	－75.51	8.58
②	－15	－15.51	—
③	6.05	5.62	—
④	12.05	11.63	—
⑤	2.08	－1.22	5.67

2.2　光频梳变频仿真

利用 Optisystem15.0 软件搭建了上变频链路进行仿真，系统结构如图 11 所示，各元器件参数配置如表 2 所示。

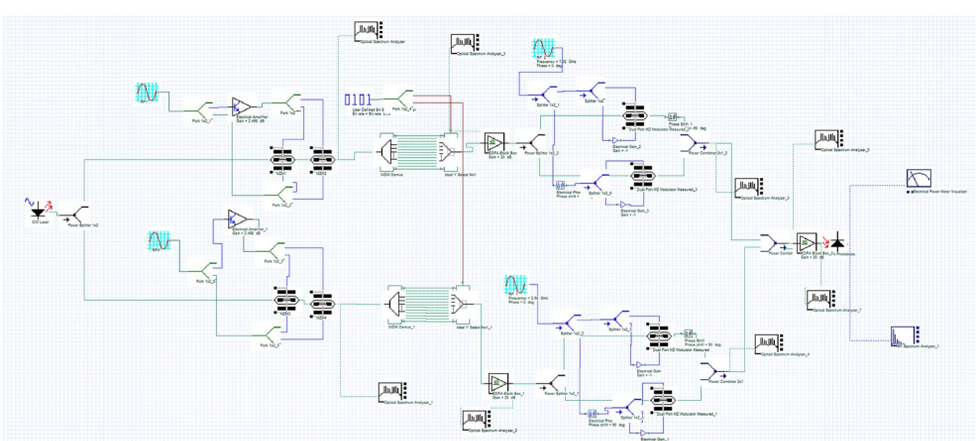

图 11　光频梳上变频仿真结构图

Fig.11　Simulation schematic diagram of optical frequency comb up-conversion

表2 各元器件参数配置表

Table 2 Component parameters and specifications

Parameter	Value	Parameter	Value
Laser frequency/THz	193.1	Laser linewidth/MHz	5
Laser output power/dBm	15	Photodetector responsivity/(A·W^{-1})	0.6
Erbium-doped fiber amplifier gain/dB	20	Erbium-doped fiber amplifier noise figure/dB	4
Wavelength demultiplexer 1 channel spacing/GHz	10	RF1 frequency/GHz	10
Wavelength demultiplexer 2 channel spacing/GHz	11	RF2 frequency/GHz	11

在仿真平台中，连续波激光器输出光载波经光分路器等分至上下两个支路，分别作为频移支路和载波支路。激光器输出光信号中心频率为193.1 THz，线宽为5 MHz，输出功率为15 dBm。两路光载波分别注入级联双驱动马赫-曾德尔调制器，通过独立调控射频信号RF1和RF2的频率，形成具有相同中心波长但梳齿间隔不同的本振光频梳与载波光频梳。其中，RF1与RF2输出信号频率分别为10 GHz与11 GHz，幅值设定为6 V。通过精细调节电放大器增益，确保级联双驱动马赫-曾德尔调制器的上下臂输入信号满足幅度差为$V_\pi/2$，其中调制器半波电压V_π=6 V，消光比为35 dB。同时，通过校准调制器两臂的直流偏置电压，使上下臂相位差满足π/2。满足以上条件后，上下支路调制器输出的本振光频梳与载波光频梳光谱图如图12所示，光频梳梳齿轮廓清晰可辨，谱线平坦度较为优异(5 dB波动带宽内稳定维持23根有效梳齿)，且载波噪声比优于30 dB。

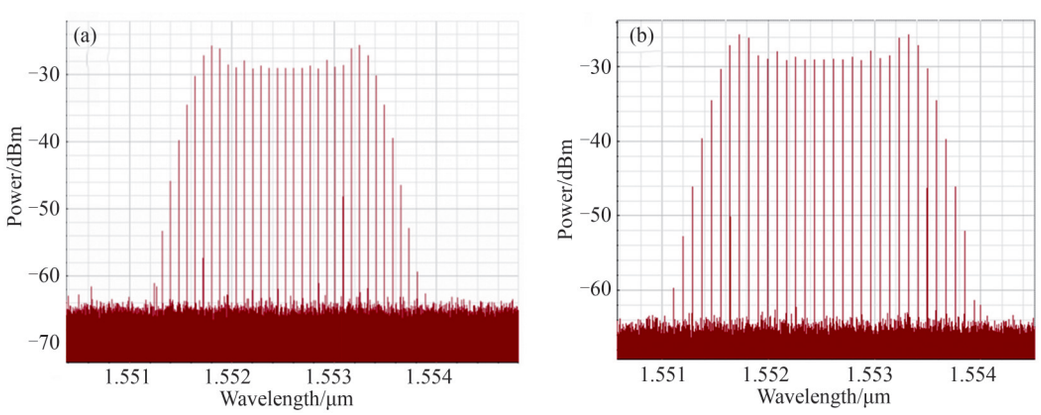

图12 光频梳光谱图。(a)上支路；(b)下支路

Fig.12 Optical frequency comb spectrum. (a) Upper branch; (b) Lower branch

然后，本振光频梳和载波光频梳分别进入上下支路中的1×13波分解复用器和13×1光开关进行信道化，利用掺铒光纤放大器对输出梳齿进行放大。设置波分解复用器通道抑制比为25 dB，通道间隔频率分别与光频梳梳齿间距对应。以上下支路波分解复用器的第一个通道为例，设置掺铒光纤放大器增益为20 dB，最终得到本振和载波的光谱图如图13所示。

将频移信号设置为7.32 GHz单音信号，下支路输入信号为2.68 GHz单音信号，输入90°电桥一分为二后，分别输入上下支路IQ调制器的两个端口中。设置IQ调制器消光比为35 dB，上支路调制器的相位为−90°，下支路则为90°。最终信道1中IQ调制器对应输出载波抑制单边带调制后的信号光谱图如图14所示。从光谱图中可以看出，上支路保留了左侧边带，下支路则保留了右侧边带，信道的残留载波抑制比约为25 dB，具有较好的隔离度。

上下两支路调制后通过合路器合路，输入到掺铒光纤放大器中进行功率补偿，得到输出信号光谱图如图15(a)所示。补偿后信号输入到PD中进行光电转换，得到信道1输出的射频信号频谱图如图15(b)所示，杂散抑制比约为21 dB。

对4～16 GHz的每个通道进行遍历，得到最终输出各个通道的频谱图如图16所示。从图中可以看出，最终输出信号频率为4～16 GHz，通道间隔为1 GHz，杂散抑制比约为20 dB，带内(4～16 GHz)平坦度小于等于4 dB。

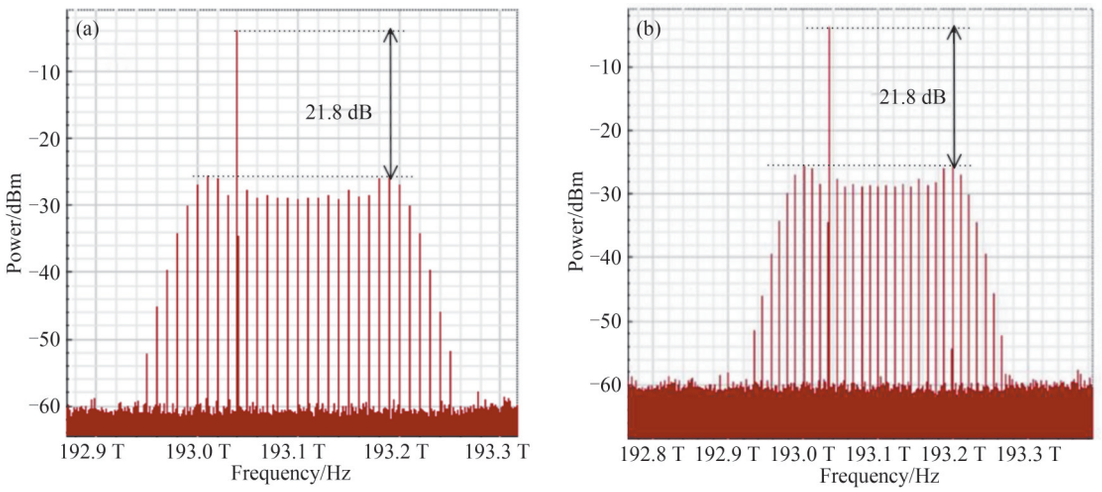

图 13　仿真后的光谱图。(a)信道 1 本振;(b)信道 1 载波光谱

Fig.13　Spectrum from simulation. (a) Channel 1 Local Oscillator (LO); (b) Channel 1 carrier spectrum

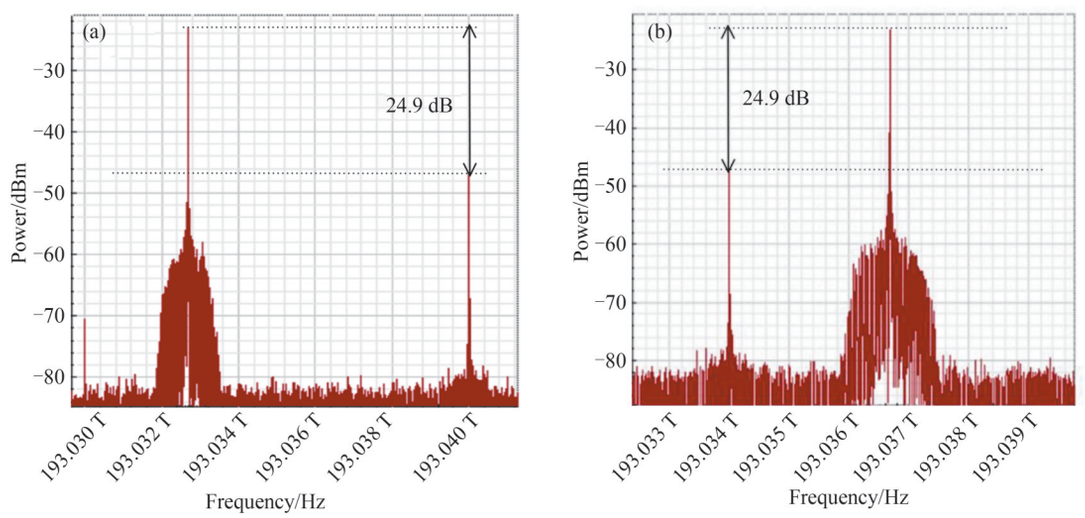

图 14　调制后光谱图。(a)信道 1 本振;(b)信道 1 载波

Fig.14　Optical spectra after modulation. (a) Channel 1 Local Oscillator (LO); (b) Channel 1 carrier

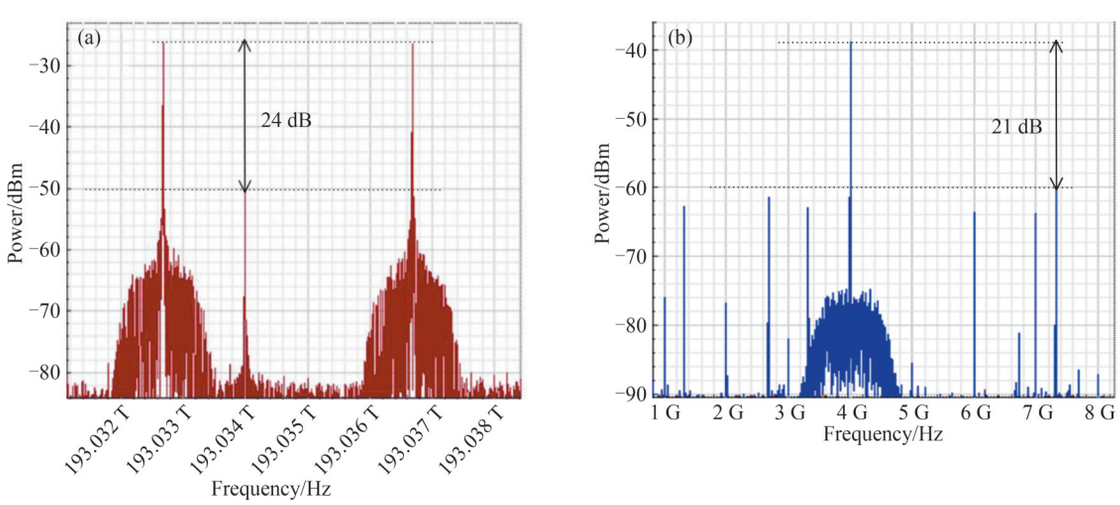

图 15　补偿后的光谱图。(a)信道 1 补偿后光谱图;(b)拍频后的光谱图

Fig.15　Spectrum after compensation. (a) Compensated optical spectrum of channel 1; (b) Optical spectrum after heterodyning

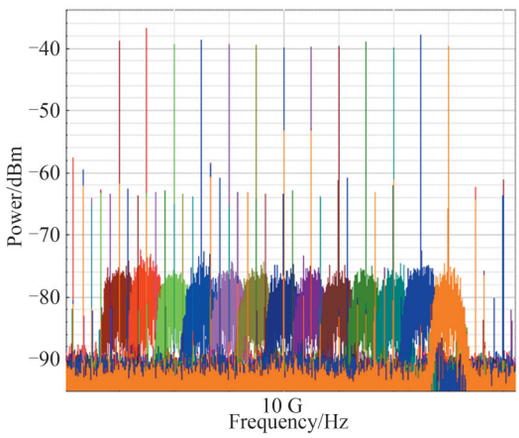

图 16 各通道输出信号频谱图

Fig.16 Output signal spectra of all channels

为了提高信号的输出功率，在IQ调制器前增加了增益为29 dB的LNA，并在PD后增加了电放大器对功率进行进一步补偿，得到IQ调制器最终输出的载波抑制单边带调制后的宽带信号如图17(a)所示，由于调制了宽带信号，载波抑制比下降至20 dB左右；最终得到的各个通道宽带射频信号频谱图如图17(b)所示，从图中可以看出，调制了宽带信号以后，杂散抑制比明显下降，信号带内平坦度恶化(~6 dB)，信号质量变差。

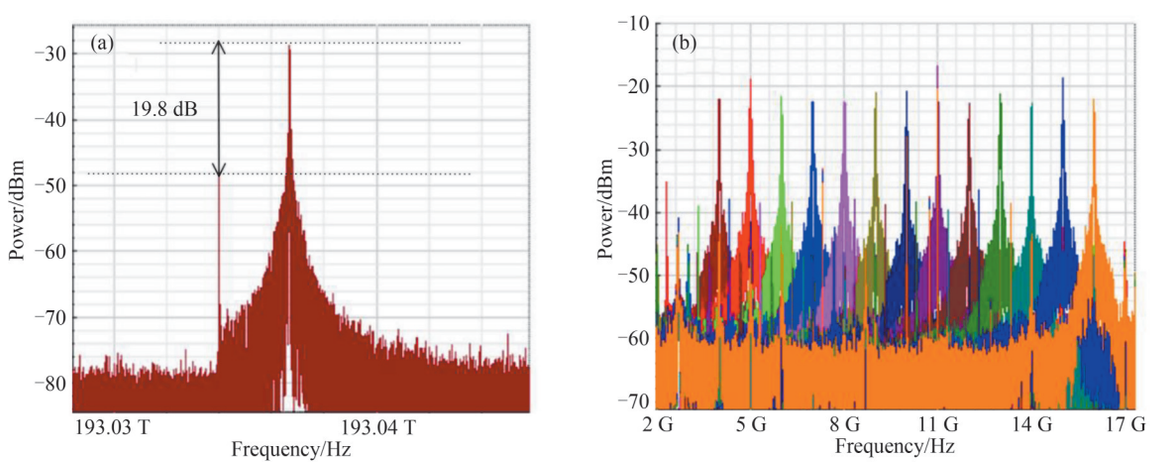

图 17 调制宽带信号后输出的光谱图。(a)载波调制后光谱图；(b)各通道输出信号频谱图

Fig.17 Spectrum of a modulated wideband signal. (a) Optical spectrum of modulated carrier; (b) Output signal spectra of all channels

从上述分析可以看出，产生杂散的主要原因是波分解复用器和载波抑制单边带调制过程中残留的信号在PD中拍频导致的。为此，为了提升杂散抑制比，提高信号质量，需要对波分解复用器和IQ调制器的通道抑制比以及消光比进行分析。由于仿真中使用的调制器均为高消光比调制器，消光比为36 dB，现有商用市场中已无更高消光比的调制器，因此我们只能通过提升波分解复用器通道抑制比来提升杂散抑制比。通过设置其他参数不变，改变波分解复用器通道抑制比，分析输出信号的杂散抑制比，得到的结果如图18所示。从图中可以看出，随着波分解复用器通道抑制比的增加，系统输出信号杂散抑制比不断提高。当通道抑制比为40 dB左右时，曲线饱和，杂散抑制比达到最高且无法进一步提升。

由于商用非标准波分解复用器的通道抑制比目前最高只能达到20 dB，因此为了提高波分解复用器通道抑制比，我们可以利用光注入锁定放大或者额外增加一个波分解复用器来提升通道抑制比。对应通道平坦度的优化，可以通过在每个通道增加一个可调光衰减器，对输出信号的功率进行预补偿来提升带内通道平坦度。

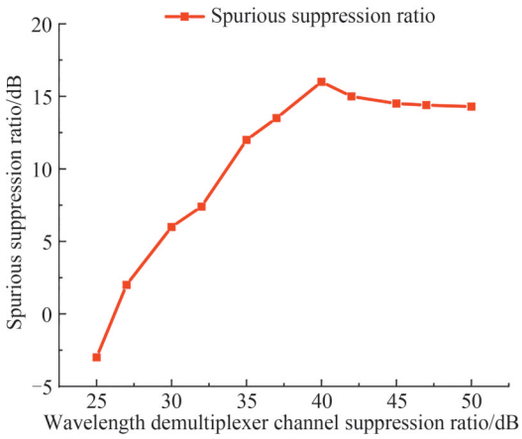

图 18　杂散抑制随波分解复用器通道抑制比变化曲线

Fig.18　Variation curve of spurious suppression versus wavelength demultiplexer channel suppression ratio

3　结论

针对传统超视距通信在跨频段、超宽带与多通道并行处理等方面存在的电子瓶颈，结合微波光子学的技术优势，系统开展了基于微波光子技术的超视距通信系统关键技术研究与系统设计工作，并完成整体通信链路的仿真，取得如下进展：在微波光子相控阵链路方面，完成了链路模型的构建、理论分析与系统仿真，在信噪比恶化低于 3 dB 的条件下，实现了超视距通信系统在 4～16 GHz 跨频段范围内的多信道并行处理；在光频梳频率变换方面，建立了上下变频系统模型并完成理论分析，在此基础上对光频梳上变频过程进行了仿真验证，通过 23 根光频梳实现了 13 个波道的可重构切换功能，成功将 336 MHz 中频信号上变频至 4～16 GHz 频段，通道间隔为 1 GHz，杂散抑制比优于 20 dB，带内（4～16 GHz）幅度起伏不超过 4 dB，实现了 MHz 量级频率的精确调控。

然而，该技术体系从仿真验证迈向实际工程部署仍面临一系列严峻挑战。在环境适应性方面，光子与射频器件对温度波动及机械振动极为敏感，可能导致光频梳梳齿偏移、调制器偏置点漂移以及通道相位失配，进而引起系统性能显著退化。在成本与集成层面，高频宽带电光调制器、可调谐窄线宽激光器及多通道光延时网络等核心部件价格昂贵，且混合光电系统的封装、耦合与散热设计复杂度高，难以满足规模化应用的需求。此外，仿真中实现的杂散抑制、带内平坦度等关键指标在实际复杂电磁环境与多物理场耦合作用下可能难以保持，对系统的长期稳定性构成重要挑战。

针对实际工程部署中面临的挑战，未来的研究工作将聚焦在两个方向：一是通过硅基光电子、异质集成等先进工艺实现器件与系统的芯片化、模块化，从根本上缩小体积、降低功耗与成本；二是引入人工智能与数字孪生技术，构建具有在线学习能力的智能调控系统，实现对温度漂移、非线性失真及通道不一致性的实时监测与动态补偿，显著提升系统在复杂环境下的鲁棒性。通过探索研究多学科交叉与全链条创新，实现从仿真验证、原理样机到外场应用的全过程突破，使微波光子技术真正服务于未来高速、抗干扰、超视距的通信需求。

参考文献

[1] KINGSLEY S, QUEGAN S. Understanding radar systems[M]. SciTech Publishing, 1992.
[2] SKOLNIK M I. Introduction to radar systems[M]. McGraw-Hill, 2001.
[3] 张明，王建军. 军事通信技术发展趋势分析[J]. 通信技术，2020，53(2)：1-5.
[4] YAO Jianping. Microwave photonics[J]. Science China Information Sciences，2022，12(65)：221401.
[5] YAO Jianping. Microwave photonics[J]. Journal of Lightwave Technology, 2009, 27(3): 314-335.
[6] MARPAUNG D, ROELOFFZEN C, HEIDEMAN R, et al. Integrated microwave photonics[J]. Laser & Photonics Reviews, 2013, 7(4): 506-538.
[7] SEEDS A J, WILLIAMS K J. Microwave photonics[J]. Journal of Lightwave Technology, 2006, 24(12): 4628-4641.
[8] CAPMANY J, NOVAK D. Microwave photonics combines two worlds[J]. Nature Photonics, 2007, 1(6): 319-330.
[9] LI Jinxin, XIE Yuhang, WO Jianghai, et al. Multiband microwave photonic radar with increased target detection ability[J].

Optics Letters, 2025, 50:4094-4097.
[10] SHAO Shuai, WU Yilin, XUE Qiyin, et al. Multi-band reconfigurable microwave photonic transceiver towards high-performance integrated radar[J]. Optics Express, 2025, 33:3654-3669.
[11] FU Yufei, CAI Jiazhen, MA Jingcan, et al. Hybrid digital-analog beamforming architecture for rapid beam steering based on microwave photonics[J]. Optics Letters, 2025, 50:4026-4029.
[12] CHEN Guchang, LI Chenyuan, XIE Xiangzhi, et al. Microwave photonics channelized receiver with high phase stability [J]. Optics Express, 2025, 33:23668-23677.
[13] SHI Jingzhan, WANG Yian, ZHU Dan, et al. A microwave photonic FMCW radar with suppressed phase noise based on equal phase interval sampling[J]. IEEE Photonics Technology Letters, 2025, 37(4):195-198.
[14] WANG Xiangchuan, CAO Fengting, MA Cong, et al. Dual-band coherent microwave photonic radar using linear frequency modulated signals with arbitrary chirp rates[J]. IEEE Journal of Selected Topics in Quantum Electronics, 2023, 29(6):1-9.
[15] CHEN Bo, DONG Qunfeng, CAO Biao, et al. Broadband microwave photonic channelizer with 18 channels based on acousto-optic frequency shifter[J]. Photonics, 2023, 10(2):107.
[16] YANG Jiasi, ZHENG Zhennan, XUE Hanxiao, et al. Low-loss microwave photonic switching for satellite communication [J]. Optics Letters, 2023, 48: 3821-3824.
[17] HE Yuanzhi, TAN Qinggui, WEN Aijun, et al. Satellite communication payload based on microwave photonics: benefits, architecture, and technologies[J]. IEEE Wireless Communications, 2024,31(1):164-171.
[18] ZHU Sha, FAN Xiaojie, LI Ming, et al. Microwave photonic frequency down-conversion and channel switching for satellite communication[J]. Optics Letters, 2020, 45:5000-5003.
[19] LIU Qidi, FOK MP. Ultrafast and wideband microwave photonic frequency-hopping systems: a review. applied sciences [J]. Applied Sciences, 2020, 10(2):521.
[20] SHI Fangjing, FAN Yangyu, MA Boyuan, et al. A microwave photonic channelized receiver with self-interference cancellation[J]. Journal of Lightwave Technology, 2023,41(2): 627-636.
[21] MATHUR M, RAI J, SRIDHAR N. Design and validation of rugged microwave photonic network for phased-array radar [J]. Fiber and Integrated Optics, 2015,34(5-6): 243-258.
[22] LUAN Yuchen, YANG Tian, REN Jian, et al. Broadband beam-scanning phased array based on microwave photonics [J]. Electronics, 2024, 13(7):1278.
[23] PODBREGAR L, BATAGELJ B, BLATNIK A, et al. Advances in and applications of microwave photonics in radar systems[J]. Photonics, 2025, 12(6):529.
[24] FANG Xiao, BAI Ming, YE Xiuzhu, et al. Ultra-broadband microwave frequency down-conversion based on optical frequency comb[J]. Optics Express, 2015, 23(13): 17111-17119.
[25] LIN Tao, ZHAO Shanghong, ZHU Zihang, et al. Photonic microwave multi-band frequency conversion scheme based on dual-OFCs for satellite communication[C]. 2016 15th International Conference on Optical Communications and Networks (ICOCN), 2016.
[26] CHEN Feengyu, ZHU Xiiaoqi, CHEN Ziyang. Microwave photonic down conversion system with programmable frequency response utilizing optical frequency comb[C]. 2017 Asia Communications and Photonics Conference (ACP), 2017.
[27] YAO Jianping. Microwave photonic phased array antenna[J]. Journal of Lightwave Technology, 2009, 27(7): 314-335.
[28] PASCHOTTA R. Encyclopedia of laser physics and technology[M]. Wiley-VCH, 2008.
[29] CHAN E, MINASIAN R. Tunable photonic true-time delay beamforming based on optimized dispersion-compensating fiber modules[J]. Journal of Lightwave Technology, 2013, 31(5): 721-727.
[30] LIU Yuan, LI Zihang, ZHANG Feng, et al. Wideband beamforming based on optical true time delay with dispersion-induced squint compensation[J]. Optics Express, 2019, 27(11): 15589-15600.
[31] ZHU Dan, PAN Shengwei. Integrated optical beamforming network for phased array antennas[J]. IEEE Journal of Selected Topics in Quantum Electronics, 2021, 28(3): 1-13.
[32] COX III, ACKERMAN E, BETTS G, et al. Limits on the performance of RF-over-fiber links and their impact on device design[J]. IEEE Transactions on Microwave Theory and Techniques, 2006, 54(2): 906-920.
[33] WILLIAMS K, ESMAN R. Design considerations for high-current photodetectors[J]. Journal of Lightwave Technology, 1999, 17(8): 1443-1454.
[34] DARCIE T, TUCKER R. Intermodulation and harmonic distortion in InGaAsP lasers[J]. Electronics Letters, 1985, 21(16): 665-666.
[35] URICK V, WILLIAMS K, MCKINNEY J. Fundamentals of microwave photonics[M]. John Wiley & Sons, 2015: 45-48.
[36] CLARK T, DENNIS M. System trade-offs for microwave photonic links[C]. 2011 International Topical Meeting on

Microwave Photonics, IEEE, 2011: 1-4.
[37] DEVGAN P, TANG R, URICK V, et al. Effects of laser relative intensity noise on the performance of analog photonic links[J]. IEEE Journal of Selected Topics in Quantum Electronics, 2018, 25(3): 1-9.

Advanced Over-the-horizon Communications with Microwave Photonic Technologies (Invited)

WANG Luqiang[1,2], PU Tao[1], LI Jin[1], ZHENG Jilin[1], ZHOU Hua[1], ZHAO Xiaolong[1], LIU Shuya[1], YU Jingxi[2]

(1 *Army Engineering University of PLA, Nanjing* 210001, *China*)
(2 *The Fifty-fourth Research Institute of China Electronics Technology Group Corporation, Shijiazhuang* 050002, *China*)

Abstract: This research is driven by the critical need to overcome the inherent limitations of conventional Radio Frequency (RF)-based Over-The-Horizon (OTH) communication systems. Traditional systems, which rely on the propagation of microwave signals through the atmosphere or via ionospheric reflection, face significant challenges that constrain their performance in modern, high-demand scenarios. These challenges include severely limited bandwidth capacity, which restricts data throughput; vulnerability to both intentional jamming and unintentional electromagnetic interference, compromising reliability; and a lack of operational flexibility, making real-time reconfiguration and multi-channel parallel processing difficult. Furthermore, achieving wideband, cross-frequency operation often necessitates complex, bulky, and power-intensive electronic components. The primary objective of this work is to conceptualize, design, and validate a next-generation OTH communication system architecture that fundamentally transcends these electronic bottlenecks. By strategically integrating the field of microwave photonics—which utilizes light to generate, process, and distribute microwave signals—this study aims to create a system prototype capable of delivering unprecedented levels of bandwidth, robust anti-interference performance, and dynamic reconfigurability. The ultimate goal is to establish a concrete technological foundation for future OTH platforms that can meet the escalating demands for secure, high-capacity, and resilient long-distance tactical and strategic communication links.

To achieve the stated objectives, a comprehensive system design and simulation-based research methodology was employed, centered on a novel architecture that synergizes three core microwave photonic subsystems. The system′s front-end is a microwave photonic phased-array antenna. This antenna comprises 64 independent elements designed to simultaneously capture weak wireless signals from free space. The received RF signals from each element are first amplified by a dedicated Low-Noise Amplifier (LNA) to mitigate front-end noise. Subsequently, each amplified RF signal is used to directly modulate the intensity of a continuous-wave optical carrier generated by a Directly Modulated Laser (DML), thereby translating the electrical signals into the optical domain. This process creates 64 parallel optical RF channels. A critical innovation lies in the beamforming network. The 64 optical signals are fed into a tunable optical delay and attenuation module. A centralized digital control unit precisely and independently adjusts the time delay and attenuation for each of the 64 optical paths. This optical True-Time-Delay (TTD) approach is frequency-independent, enabling wideband, squint-free beam steering and shaping. The individually processed optical signals are then coherently combined via a Wavelength Division Multiplexing (WDM) stage, effectively synthesizing the desired radiation pattern in the optical domain before detection. The combined optical beam is converted back into a consolidated electrical RF signal using a high-speed Photodetector (PD). This aggregated RF signal is then routed to the second core subsystem: the microwave photonic frequency conversion unit. The heart of this unit is a coherent dual Optical Frequency Comb (OFC) setup. One OFC serves as a multi-wavelength Local Oscillator (LO), while the other is used for signal modulation. Electro-Optic Modulators (EOMs) are used for precise signal imprinting and frequency shifting. A key technique implemented is Carrier-Suppressed Single-Sideband (CS-SSB) modulation, achieved by carefully biasing the EOMs, which eliminates LO leakage and provides excellent channel isolation. This setup allows for the simultaneous up-conversion or down-

conversion of multiple RF channels across a ultra-wide bandwidth. The final subsystem is an integrated communication terminal, which performs demodulation, decoding, and protocol processing on the recovered baseband signals. The feasibility and performance of this integrated architecture were rigorously validated through detailed theoretical modeling and extensive link-level simulations using the industry-standard Optisystem software, which models the complex interactions between optical and RF components.

The simulation and analysis of the proposed microwave photonic OTH system yielded highly promising results across multiple performance dimensions, confirming the effectiveness of the chosen architectural approach. Core Communication Performance: The system successfully demonstrated stable and high-fidelity signal transmission across the entire 4～16 GHz operational bandwidth. Within this spectrum, a sustained communication data rate of 200 Mbps was achieved, representing a significant improvement over typical narrowband OTH links and validating the system′s high-bandwidth capability. Reconfigurable Channelized Processing: A major accomplishment was the implementation of reconfigurable microwave photonic channelized frequency conversion. The system possesses the ability to dynamically process signals across 13 independent wavelength channels. This channelization allows for simultaneous, parallel handling of multiple communication streams or signal sub-bands within the wide RF aperture, greatly enhancing spectral efficiency and multi-user capacity. Phased Array Link Performance: For the 64-element microwave photonic phased array link, detailed simulation confirmed that multi-channel parallel processing was feasible with minimal signal quality degradation. Critically, the complex beamforming and signal combining processes were achieved with a signal-to-noise ratio (SNR) degradation of less than 3 dB, indicating highly efficient optical processing and minimal noise introduction from the photonic beamforming network. Optical Frequency Comb Conversion Performance: The dual-OFC frequency conversion subsystem exhibited exceptional precision and spectral purity. Using an array of 23 finely spaced optical comb lines, the system realized the reconfigurable switching functionality for the 13 channels. Specifically, it accomplished the up-conversion of a 336 MHz Intermediate Frequency (IF) signal to the target 4～16 GHz RF band. The converted spectrum showed excellent characteristics: a well-defined channel spacing of 1 GHz, a spurious suppression ratio better than 20 dB (indicating minimal unwanted harmonic generation), and a high in-band amplitude flatness with fluctuations not exceeding 4 dB across the entire 12 GHz range. This suite of metrics confirms the system′s ability to perform precise, MHz-level frequency control and management with high spectral integrity.

In conclusion, this research has successfully established the technical viability and superior potential of a microwave photonic approach to revolutionizing over-the-horizon communication. The proposed and analyzed system architecture, integrating a photonic phased array, a dual-optical-frequency-comb-based channelizer, and an integrated terminal, directly addresses and overcomes the fundamental bandwidth, interference, and flexibility constraints inherent in traditional electronic OTH systems. The simulation results provide compelling evidence that such a system can deliver wideband (4～16 GHz), high-data-rate (200 Mbps), multi-channel (13 channels), and reconfigurable communication links with high spectral purity and efficient beamforming. Beyond the immediate performance metrics, this work lays a critical and substantial foundation for the future engineering and deployment of advanced OTH communication systems. It demonstrates a clear pathway toward building more secure, resilient, and high-capacity strategic communication infrastructures. Future work will naturally focus on the practical implementation of this architecture, including the development of integrated photonic chips to reduce size, weight, and power consumption (SWaP), experimental validation in real-world propagation environments, and the exploration of advanced signal processing algorithms to further enhance performance. This study marks a significant step forward in the convergence of photonics and wireless communications for national security and civilian long-range connectivity applications.

Key words: Microwave photonics; Over-the-horizon communication; Phased array; Optical frequency comb; Frequency conversion

OCIS Codes: 350.3950; 350.4010; 060.2630; 060.4230

CSTR: 32255.14.gzxb20265503.0355110

Foundation item: National Natural Science Foundation of China (62201615,62371470)